

ABSTRACT

Title of dissertation: Measuring topology of BECs
in a synthetic dimensions lattice

Dina Genkina
Doctor of Philosophy, 2018

Dissertation directed by: Professor Ian Spielman
Department of Physics

Measuring topology of BECs in a synthetic dimensions lattice

by

Dina Genkina

Dissertation submitted to the Faculty of the Graduate School of the
University of Maryland, College Park in partial fulfillment
of the requirements for the degree of
Doctor of Philosophy
2018

Advisory Committee:
Professor Ian Spielman, Chair/Advisor

© Copyright by
Dina Genkina
2018

Table of Contents

| | |
|---|----|
| List of Tables | 6 |
| List of Figures | 7 |
| 2 Atom Light Interactions | 1 |
| 2.1 Near-resonant atom-light interaction | 1 |
| 2.2 Absorption imaging | 2 |
| 2.3 One dimensional optical lattices | 5 |
| 2.3.1 Far off-resonant atom-light interaction | 5 |
| 2.3.2 Lattice Hamiltonian | 7 |
| 2.3.3 Tight binding approximation | 11 |
| 2.3.4 Pulsing vs adiabatic loading of the lattice | 12 |
| 2.4 Raman and rf coupling | 17 |
| 2.4.1 Hyperfine structure | 17 |
| 2.4.2 Rf coupling Hamiltonian | 19 |
| 2.4.3 Raman coupling Hamiltonian | 21 |
| 2.4.4 Calibration of Raman and Rf dressed states | 24 |
| 6 Synthetic Magnetic Fields in Synthetic Dimensions | 30 |
| 6.1 Synthetic dimensions setup | 31 |
| 6.2 Hamiltonian of the effective 2-D system | 34 |
| 6.2.1 Hamiltonian | 34 |
| 6.2.2 Band structure | 36 |
| 6.2.3 Calibration | 39 |
| 6.2.4 Tight binding approximation | 42 |
| 6.3 Eigenstates of the synthetic 2-D lattice | 44 |
| 6.4 Chiral edge currents | 46 |
| 6.5 Observation of skipping orbits | 49 |
| Bibliography | 52 |

List of Tables

List of Figures

| | | |
|---|---|----|
| 1 | Absorption imaging. (a) Near resonant probe light illuminates the atoms, and the transmitted light (containing a shadow of the atoms) is imaged on the camera. A second image taken with no atoms provides a reference. (b) The probe beam is partially absorbed as it traverses the cloud, and the intensity seen by atoms further along the imaging direction e_z is lowered. (c) An atomic cloud illuminated by a probe light field absorbs photons from the probe and re-emits them in all directions. This process results in a net acceleration of the cloud in the direction of the probe light as well as diffusive spreading in the transverse directions. | 3 |
| 2 | Lattice band structure in the extended zone scheme. The dashed lines represent the limit of zero lattice depth, with the regular parabolic dispersion relation of a free particle repeating with reciprocal lattice period. The solid lines are the dispersion relation at $V_0 = 4.0E_L$, showing the opening of gaps at crossings of the zero lattice depth bands. The black lines demarcate the first Brillouin zone. | 10 |
| 3 | Lattice pulsing. (a) Lattice depth as a function of time during a pulsing experiment. The lattice is turned on instantaneously at $t = 0$ and held on for a variable amount of time until being turned off instantaneously at a final time $t = t_f$. (b) Atomic population before $t = 0$. The dispersion relation is that of a free particle, and all of the atoms start out at $q = 0$ in the lowest energy level. Here, the area of the dots is proportional to the fractional population in the energy state. (c) Atomic population after the lattice is turned on for a lattice depth of $V_0 = 8.0E_L$. The energy spectrum now shows the lattice band structure, and some atomic population is projected onto the excited bands. (d) Atomic population after the lattice is snapped off at $t_f = 150 \mu s$. The wavefunction is projected back onto the bare states, with some fraction (blue circle) in the lowest band at $k = 0$ and some fraction in the excited band, with equal population being projected onto the $k = 2k_L$ (green) and $k = -2k_L$ (red). | 14 |

| | | |
|---|---|----|
| 4 | Lattice pulsing for calibration. (a) An example time-of-flight image from a pulsing experiment. The three different clouds are different momentum orders. (b) Fractional populations in the different momentum orders as a function of pulsing time at a low lattice power. Data is indicated by dots and best fit theory is represented by lines. The lattice depth from fit is $V_0 = 5.57 \pm 0.07 E_L$. (c) Fractional populations in the different momentum orders as a function of pulsing time at a higher lattice power. Data is indicated by dots and best fit theory is represented by lines. The lattice depth from fit is $V_0 = 12.69 \pm 0.07 E_L$. | 15 |
| 5 | Adiabatic lattice loading. (a) Lattice depth as a function of time during adiabatic turn-on. The lattice is ramped on starting at $t = 0$, slowly increasing to a final lattice depth and turned off instantaneously at a final time $t = t_f$. (b) Atomic population before $t = 0$. All atoms are at $k = 0$ in the lowest bare band. (c) Atomic population after the lattice is turned on adiabatically to a lattice depth of $V_0 = 8.0 E_L$. All atoms remain in the lowest band, but the band is no longer bare. (d) Atomic population after the lattice is snapped off. The wavefunction is projected back onto the bare states, with some fraction (blue circle) in the lowest band at $k = 0$ and some fraction in the excited band, with equal population being projected onto the $k = 2k_L$ (green) and $k = -2k_L$ (red). Since the lowest lattice band is a superposition of bare bands, some atoms are excited to the higher bare bands. | 16 |
| 6 | Energy structure of hyperfine states of the ground state of ^{87}Rb as a function of external magnetic field strength in Gauss. Figure from ref. [1] | 18 |
| 7 | Raman and rf coupling schematic. (a) Beam geometry of the Raman beams and rf relative to the external field. The Raman beams have a frequency difference $\Delta\omega$, and are linearly polarized in perpendicular directions. (b) Level structure of both Raman and Rf coupling for hyperfine states of the $F = 1$ manifold. The hyperfine splitting separates the levels by an energy $\hbar\omega_z$. The quadratic Zeeman shift ϵ lowers the energy of the $m_F = 0$ state, and the detuning δ of either the Raman or the rf fields shifts the energies of the $m_F = \pm 1$ states. Raman transitions are two-photon, exciting up to a virtual state and coming back down to an adjacent hyperfine state, with an accompanying momentum transfer. Rf couples adjacent hyperfine states directly. Figure taken from ref. [2] | 20 |
| 8 | Band structure of the rf Hamiltonian, Eq. 2.28, in momentum space. For all plots, the quadratic Zeeman shift $\hbar\epsilon = 0.04 E_R$, and the color represents magnetization, labeled by the colorbar. (a) $\hbar\Omega = 0$, $\hbar\delta = 0$. No coupling or detuning is present, so the only separation between the bands is due to the quadratic shift $\hbar\epsilon$. (b) $\hbar\Omega = 5.0 E_R$, $\hbar\delta = 0$. (c) $\hbar\Omega = 0$, $\hbar\delta = 1.0 E_R$. Even though the coupling strength is zero, the bands are separated by the detuning. (d) $\hbar\Omega = 5.0 E_R$, $\hbar\delta = 1.0 E_R$. | 22 |

| | | |
|----|---|----|
| 9 | Band structure of the Raman Hamiltonian, Eq. 2.31, in momentum space. For all plots, the quadratic Zeeman shift $\hbar\epsilon = 0.04E_R$, and the color represents magnetization, labeled by the colorbar. (a) $\hbar\Omega = 0$, $\hbar\delta = 0$. (b) $\hbar\Omega = 1.0E_R$, $\hbar\delta = 0$. (c) $\hbar\Omega = 5.0E_R$, $\hbar\delta = 0.0$. (d) $\hbar\Omega = 0.0$, $\hbar\delta = 1.0E_R$. (e) $\hbar\Omega = 1.0E_R$, $\hbar\delta = 1.0E_R$. (f) $\hbar\Omega = 5.0E_R$, $\hbar\delta = 1.0E_R$ | 25 |
| 10 | Pulsing on rf coupling. (a) Example time-of-flight image during an rf pulsing experiment in the $F = 1$ manifold. Spin states are separated via a Stern-Gerlach pulse along the horizontal direction. (b) Example time-of-flight image during an rf pulsing experiment in the $F = 2$ manifold. Here, 5 spin components are present. (c) Pulsing experiment in the $F = 1$ manifold. Dots represent fractional populations in different spin states measured from time-of-flight images, and lines represent best fit theory curves. Fitted parameters are $\hbar\Omega = 0.863 \pm 0.004E_R$, $\hbar\delta = -0.198 \pm 0.007E_R$. (d) Pulsing experiment in the $F = 2$ manifold. Dots represent fractional populations in different spin states measured from time-of-flight images, and lines represent best fit theory curves. Fitted parameters are $\hbar\Omega = 1.000 \pm 0.002E_R$, $\hbar\delta = -0.061 \pm 0.001E_R$. $\hbar\epsilon = 0.038E_R$ for all panels. | 27 |
| 11 | Pulsing on Raman coupling. (a) Example time-of-flight image during a Raman pulsing experiment in the $F = 1$ manifold. A Stern-Gerlach pulse during time-of-flight separates different spin components along the horizontal direction, and different momentum orders fly apart along the vertical direction. (b) Fractional population in different spin states during a Raman pulsing experiment as a function of time. Dots represent data and lines represent a best fit from theory. The fitted parameters are $\hbar\Omega = 1.47 \pm 0.01E_R$, $\hbar\delta = 0.004 \pm 0.024E_R$. The quadratic Zeeman shift was $\hbar\epsilon = 0.038E_R$ | 28 |
| 1 | Setup of effective 2-D lattice. (a) Beam geometry. The BEC is subject to a bias magnetic field B_0 in the \mathbf{e}_z direction. The 1-D lattice beam and Raman beams are both along the \mathbf{e}_x direction, and the rf field can be applied with projections onto both the \mathbf{e}_x and \mathbf{e}_y . (b) Schematic of the effective 2-D lattice. Sites along \mathbf{e}_x are formed by the 1-D optical lattice and labelled by site number j . Sites along the synthetic direction \mathbf{e}_s are formed by the spin states: 3 sites for atoms in the $F = 1$ manifold and 5 sites for atoms in $F = 2$. These sites are labelled by m . Raman transitions induce a phase shift, which can be gauge transformed into a tunneling phase along the \mathbf{e}_x direction. This leads to a net phase when hopping around a single lattice plaquette of ϕ_{AB} | 32 |

| | | |
|---|---|----|
| 2 | Band structure of the synthetic dimensions Hamiltonian, eqn. 6.4. For all panels, the detuning $\hbar\delta = 0$ and the quadratic shift $\hbar\epsilon = 0.02E_L$. (a) $F = 1$, $\hbar\Omega = 0.0$. (b) $F = 1$, $\hbar\Omega = 0.5$. (c) $F = 2$, $\hbar\Omega = 0.0$. (d) $F = 2$, $\hbar\Omega = 0.5$ | 37 |
| 3 | Calibration of synthetic dimesnions lattice. (a) Ramping procedure. The blue line represents the 1-D lattice depth as a function of time and the red line represents Raman coupling as a function of time. Both are held on for a variable amount of time t , producing Rabi oscillations. (b) Example of fractional populations in different m states as a function of time t in the $F = 1$ manifold. Dots indicate data and lines indicate the best fit to theory, with parameters $\hbar\Omega = 0.56 \pm 0.01E_L$ and $\hbar\delta = 0.029 \pm 0.002E_L$. (c) Example time-of-flight image in the $F = 1$ manifold. A Stern-Gerlach gradient pulse separates different m states along the horizontal axis, while the lattice and Raman beams give momentum along the vertical axis. (d) Example of fractional populations in different m states as a function of time t in the $F = 2$ manifold. Dots indicate data and lines indicate the best fit to theory, with parameters $\hbar\Omega = 0.61 \pm 0.002E_L$ and $\hbar\delta = 0.002 \pm 0.001E_L$. (e) Example time-of-flight image in the $F = 2$ manifold. A Stern-Gerlach gradient pulse separates different m states along the horizontal axis, while the lattice and Raman beams give momentum along the vertical axis. | 40 |
| 4 | Band structure of the tight binding versus full Hamiltonian. $V_0 = 6.0E_L$, giving $t_x = 0.1E_L$, $\hbar\delta = 0$, $\hbar\epsilon = 0.02E_L$, $\hbar\Omega = 0.5E_L$. (a) $F = 1$, fitted value $t_s = 0.154E_L$. (b) $F = 2$, fitted value $t_s = 0.284$ | 43 |
| 5 | Eigenstates of the synthetic dimensions lattice. Left column: time-of-flight images, with position along \mathbf{e}_s on the vertical axis and momentum along \mathbf{e}_s on the horizontal. Right column: fractional populations in each site m . (a,b) Rf coupling, resulting in $\phi_{AB} = 0$. (c,f) Raman coupling, resulting in $\phi_{AB} > 0$, adiabatically loaded from the $m_F = 1$ state. (d,g) Raman coupling, resulting in $\phi_{AB} > 0$, adiabatically loaded from the $m_F = 0$ state. (c,f) Raman coupling, resulting in $\phi_{AB} > 0$, adiabatically loaded from the $m_F = -1$ state. | 45 |

- 6 Measuring chiral currents in synthetic dimensions. (a) Schematic of the formation of chiral currents when the system is loaded into the bulk $m = 0$ site and tunneling along \mathbf{e}_s is turned on suddenly. (b) Fractional population in each spin state as a function of time for a system with $\phi_{AB} > 0$. Dots represent data and lines represent theory, with parameters $\hbar\Omega = 0.5E_L$, $V_0 = 6E_L$, $\hbar\delta = 0.001E_L$, and $\hbar\epsilon = 0.05E_L$. (c) Chiral current \mathcal{I} as a function of time for $\phi_{AB} > 0$ (red) $\phi_{AB} = 0$ (empty black dots) and $\phi_{AB} < 0$ (solid black). (d) Chiral current \mathcal{I} as a function of $\langle|m|\rangle$ for the three values of ϕ_{AB} . Solid lines calculated from theory, with the same parameters as in (b) for $\phi_{AB} \neq 0$, and with parameters $\hbar\Omega = 0.33E_L$, $V_0 = 6E_L$, $\hbar\delta = -0.01E_L$, and $\hbar\epsilon = 0.05E_L$ for $\phi_{AB} = 0$. (e) Peak chiral current \mathcal{I}_{\max} as a function of tunneling asymmetry t_s/t_x . Inset: slope of best fit lines of current \mathcal{I} as a function of $\langle|m|\rangle$ (as in (d)) as a function of tunneling asymmetry t_s/t_x : nearly independent. 48
- 7 Imaging skipping orbits. (a) Schematic of pulsing experiment when atoms are initialized on the edge. (b) Schematic of the tilted box potential applied along the synthetic direction. (c) Expectation value of position along \mathbf{e}_s , $\langle m \rangle$, as a function of pulse time for atoms initialized in the $m = +1$ (red) and $m = -1$ (blue) states. Dots represent data and lines are from theory with parameters $\hbar\Omega = 0.41E_L$, $V_0 = 5.2E_L$, $\hbar\delta = \pm 0.087E_L$, and $\hbar\epsilon = 0.13E_L$. (d) Expectation value of the group velocity along \mathbf{e}_x , $\langle v_x \rangle$, for the same data as in (c). (e) Expectation value of displacement along \mathbf{e}_x , $\langle \delta j \rangle$ in units of lattice spacing, for the same data as in (c) and (d). The displacement was obtained by integrating $\langle v_x/a \rangle$, where a is the period of the optical lattice. Atoms initialized in $m = -1$ performed skipping orbits to the left, while atoms starting in $m = +1$ travelled to the right. 50

Chapter 6: Synthetic Magnetic Fields in Synthetic Dimensions

In condensed matter, 2-D systems in high fields have proved to be of great technological use and scientific interest. The integer quantum Hall effect (IQHE) [8], with its quantized Hall resistance, had given rise to an ultra-precise standard for resistivity. It was also one of the first examples of topology playing an important role in physics—the precise quantization of the Hall conductance is guaranteed by the non-trivial topology of the system [9]. This quantizes the magnetic flux into flux quanta of $\Phi_0 = 2\pi\hbar/e$, where e is the electron charge, and leads to a new ‘plateau’ in the resistivity when an additional quantum of flux is threaded through the system.

In the IQHE system, the underlying lattice structure of metal is effectively washed out—the magnetic flux per individual lattice plaquette is negligible. However, new physics arises when the magnetic flux per plaquette is increased to some non-negligible fraction of the flux quantum, giving rise to the Hofstadter butterfly [10]. These regimes are hard to reach experimentally, since the typical plaquette size in crystalline material is of order a square angstrom, and the magnetic field necessary to thread create a magnetic flux of Φ_0 through such a narrow area is of order $\approx 10^4$ Tesla, not accessible with current technology.

Several platforms have, however, reached the Hofstadter regime by engineering systems with large effective plaquette size, in engineered materials [11, 12], and in atomic [13–18] and optical [19] settings. Here, we use the approach of synthetic dimensions [20] to reach the Hofstadter regime. We demonstrate the non-trivial topology of the system created, and use it to image skipping orbits at the edge of

the 2-D system—a hallmark of 2-D electron systems in a semiclassical treatment.

The work described in this chapter was published in [21].

6.1 Synthetic dimensions setup

Any internal degree of freedom can be thought of as a synthetic dimension—the different internal states can be treated as sites along this synthetic direction. As long as there is some sense of distance along this direction, i.e. some of the internal states are 'nearest neighbors' while others are not, this is a meaningful treatment. In our case an effective 2-D lattice is formed by sites formed by a 1-D optical lattice along a 'real' direction, here \mathbf{e}_x , and the atom's spin states forming sites along a 'synthetic' direction, \mathbf{e}_s .

The experimental setup for this system is schematically represented in 1a. The BEC is subject to a 1-D optical lattice, formed by a retro-reflected beam of $\lambda_L = 1064nm$ along \mathbf{e}_x . A bias magnetic field B_0 along \mathbf{e}_z separates the different spin states. The spin states can be thought of as sites along a synthetic dimension even without any coupling field. However, only once a coupling field is present do they acquire a sense of distance. We couple them via rf or Raman coupling, which only couples adjacent spin states. The Raman beams illuminating the atoms are along the same \mathbf{e}_x direction as the 1-D optical lattice. The rf field has components both along the \mathbf{e}_x and \mathbf{e}_y .

Figure 1b sketches out the effective 2-D lattice created. Here, we have labelled the lattice sites along the 'real' direction \mathbf{e}_x by site index j . In the tight binding approximation, we can describe a lattice hopping between adjacent sites with tunneling amplitude t_x . Similarly, the sites along the 'synthetic' dimension are labelled by site index m (identical to spin projection quantum number m_F), and the rf or Raman coupling here plays the role of a tunneling amplitude t_s . In the case of rf coupling, there is no momentum kick associated with spin exchange, and both t_x

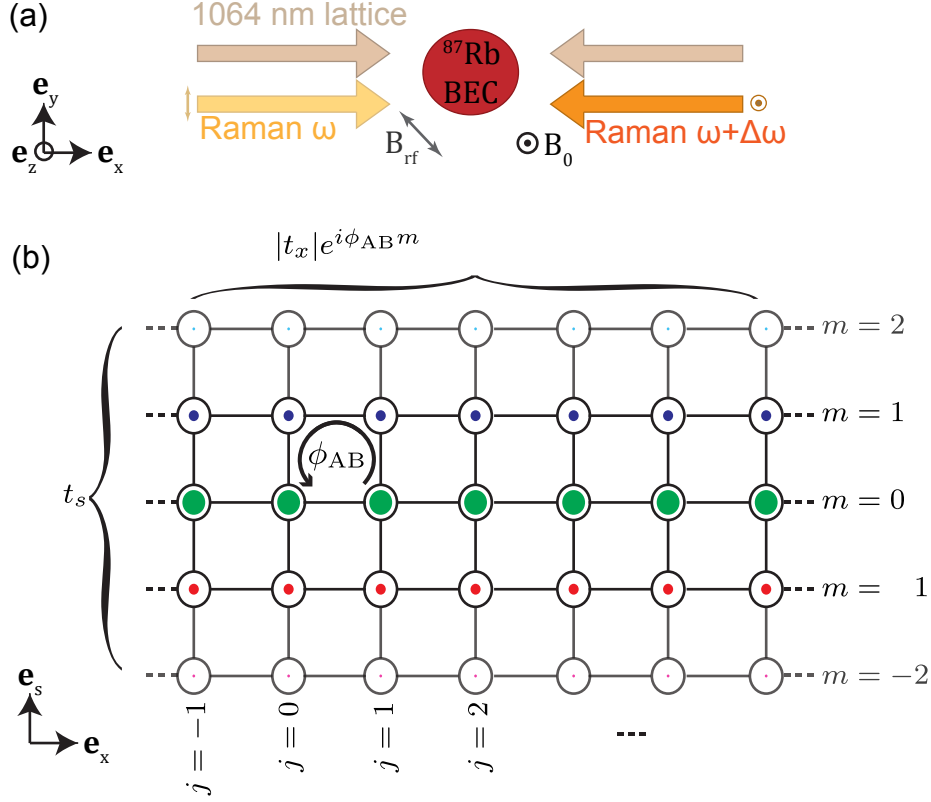


Figure 1: Setup of effective 2-D lattice. (a) Beam geometry. The BEC is subject to a bias magnetic field B_0 in the \mathbf{e}_z direction. The 1-D lattice beam and Raman beams are both along the \mathbf{e}_x direction, and the rf field can be applied with projections onto both the \mathbf{e}_x and \mathbf{e}_y . (b) Schematic of the effective 2-D lattice. Sites along \mathbf{e}_x are formed by the 1-D optical lattice and labelled by site number j . Sites along the synthetic direction \mathbf{e}_s are formed by the spin states: 3 sites for atoms in the $F = 1$ manifold and 5 sites for atoms in $F = 2$. These sites are labelled by m . Raman transitions induce a phase shift, which can be gauge transformed into a tunneling phase along the \mathbf{e}_x direction. This leads to a net phase when hopping around a single lattice plaquette of ϕ_{AB} .

and t_s are real.

In the case of Raman coupling, however, there is a momentum kick of $2k_R$ associated with every spin transfer, and therefore a phase factor of $\exp(2ik_R x)$ with every spin 'tunneling' event. Since position x is set by the 1-D lattice, $x_j = j\lambda_L/2 = j\pi/k_L$, and the space dependent phase factor is $\exp(2\pi i k_R/k_L j)$. An absolute phase change in the wavefunction is not meaningful. However, a phase acquired when going around a plaquette and coming back to the same place is meaningful, as one could imagine one atom staying at the same site and the other going around a plaquette and coming back to detect the phase difference. In this setup, the phases acquired while going around a single plaquette are, starting at some lattice site $|j, m\rangle$, are: 0 (for tunneling right to $|j+1, m\rangle$), $2\pi i k_R/k_L(j+1)$ (for tunneling up to $|j+1, m+1\rangle$), 0 (for tunneling left to $|j, m+1\rangle$) and $-2\pi i k_R/k_L j$ (for tunneling back down to $|j, m\rangle$). The total phase acquired is thus $\phi_{AB} = 2\pi k_R/k_L$, independent of the starting lattice site. Since the absolute phase does not matter and only the value of ϕ_{AB} , we can perform a phase transformation that shifts the tunneling phase onto the spatial direction, defining $t_x = |t_x|\exp(i\phi_{AB}m)$ and $t_s = |t_s|$, as labelled in Figure 1b.

To see how this phase implies an effective magnetic field, we draw an analogy to the Aharonov-Bohm effect [22, 23] from quantum mechanics. In this effect, consider an infinite solenoid with an electric current running through it. The magnetic field B in this setup exists only inside the solenoid, while the magnetic vector potential persists outside the solenoid. However, if two electrons are sent on a trajectory around the solenoid, even though they never pass through any magnetic field, they nevertheless acquire a relative phase that can be detected by interfering them with each other. This relative phase is given by $\phi_{AB} = 2\pi\Phi/\Phi_0$, where $\Phi = B * A$ is the magnetic flux through the solenoid (A is the area pierced by the magnetic field) and $\Phi_0 = h/e$ is the flux quantum, with e the electron charge. Since in our system,

the atoms acquire a phase when they perform a closed loop around a single lattice plaquette. Therefore, they behave as though there was an infinite solenoid piercing each plaquette with a magnetic field going through it, and the flux per plaquette in units of the flux quantum is $\Phi/\Phi_0 = \phi_{AB}/2\pi = k_R/k_L$. For the case of rf coupling, the phase acquired at every transition is 0 and the fluxss $\Phi/\Phi_0 = 0$.

6.2 Hamiltonian of the effective 2-D system

6.2.1 Hamiltonian

The full Hamiltonian of this system, without making the tight binding approximation, can be written down by combining the lattice Hamiltonian (eqn. 2.17) and the rf (eqn. 2.28) or Raman Hamiltonian (eqn. 2.31). To do this, we write a new basis that encompasses both the momentum and the spin degrees of freedom. For the lattice Hamiltonian, we used the momentum basis

$$\begin{pmatrix} \vdots \\ |q + 4k_L\rangle \\ |q + 2k_L\rangle \\ |q\rangle \\ |q - 2k_L\rangle \\ |q - 4k_L\rangle \\ \vdots \end{pmatrix}. \quad (6.1)$$

For the Raman Hamiltonian in the $F = 1$ manifold, we used the spin and momentum basis

$$\begin{pmatrix} |k_x - 2k_R, -1\rangle \\ |k_x, 0\rangle \\ |k_x + 2k_R, 1\rangle \end{pmatrix}. \quad (6.2)$$

In a lattice, the momentum k_x becomes crystal momentum q . For every state in the lattice basis, we now expand to three states, one for each spin state, with the appropriate momentum shifts. We obtain

$$\begin{pmatrix} \vdots \\ |q + 2k_L - 2k_R, -1\rangle \\ |q + 2k_L, 0\rangle \\ |q + 2k_L + 2k_R, 1\rangle \\ |q - 2k_R, -1\rangle \\ |q, 0\rangle \\ |q + 2k_R, 1\rangle \\ |q - 2k_L - 2k_R, -1\rangle \\ |q - 2k_L, 0\rangle \\ |q - 2k_L + 2k_R, 1\rangle \\ \vdots \end{pmatrix}. \quad (6.3)$$

In this basis, we combine the lattice and Raman Hamiltonians (ommiting the kinetic energy in the other two directions) in an infinite block matrix form as

$$H = \begin{pmatrix} \ddots & & & \\ & \mathbf{H}_{\mathbf{R}}(2k_L) & \frac{\mathbf{V}_0}{4} & \mathbf{0} \\ & \frac{\mathbf{V}_0}{4} & \mathbf{H}_{\mathbf{R}}(0) & \frac{\mathbf{V}_0}{4} \\ & \mathbf{0} & \frac{\mathbf{V}_0}{4} & \mathbf{H}_{\mathbf{R}}(-2k_L) \\ & & & \ddots \end{pmatrix}, \quad (6.4)$$

where $\mathbf{H}_R(x)$ is the Raman Hamiltonian with a momentum shift of x :

$$\mathbf{H}_R(n2k_L) = \begin{pmatrix} \frac{\hbar^2(q+n2k_L-2k_R)^2}{2m} + \hbar\delta & \hbar\Omega/2 & 0 \\ \hbar\Omega/2 & \frac{\hbar^2(q+n2k_L)^2}{2m} - \hbar\epsilon & \hbar\Omega/2 \\ 0 & \hbar\Omega/2 & \frac{\hbar^2(q+n2k_L+2k_R)^2}{2m} - \hbar\delta \end{pmatrix}, \quad (6.5)$$

the matrix $\frac{\mathbf{V}_0}{4}$ is a 3x3 diagonal matrix lattice coupling strength $\frac{V_0}{4}$ on the diagonal, and $\mathbf{0}$ is a 3x3 matrix of zeros. This extends in both directions with $\mathbf{H}_R(2nk_L)$ on the diagonal blocks and $\frac{\mathbf{V}_0}{4}$ as the first off-diagonal blocks and $\mathbf{0}$ everywhere else.

This Hamiltonian is easily extended to higher F values by replacing the Raman blocks $\mathbf{H}_R(x)$ with the corresponding Raman coupling Hamiltonian from eqn. 2.32, and extending the diagonal matrix $\frac{\mathbf{V}_0}{4}$ and the zero matrix $\mathbf{0}$ to be $(2F+1) \times (2F+1)$.

For computational convenience, we convert to lattice recoil units, $E_L = \hbar^2 k_L^2 / 2m$, $k_L = 2\pi/\lambda_L$. Then the diagonal blocks become

$$\mathbf{H}_R(n)/E_L = \begin{pmatrix} (q+n-\phi_{AB}/2\pi)^2 + \hbar\delta & \hbar\Omega/2 & 0 \\ \hbar\Omega/2 & (q+n)^2 - \hbar\epsilon & \hbar\Omega/2 \\ 0 & \hbar\Omega/2 & (q+n+\phi_{AB}/2\pi)^2 - \hbar\delta \end{pmatrix}, \quad (6.6)$$

where $\hbar\delta$, $\hbar\Omega$ and $\hbar\epsilon$ are now written in units of E_L , q is written in units of k_L and we have used the fact that $\phi_{AB}/2\pi = k_R/k_L$. The off-diagonal blocks $\frac{\mathbf{V}_0}{4}$ will be the same 3x3 diagonal matrices, with $\frac{V_0}{4}$ in units of E_L .

6.2.2 Band structure

iiiiiii HEAD

The band structure of this Hamiltonian is presented in Figure 2. Here, we have restricted ourselves to the lowest lattice band. We can do this because the energy splitting between the lowest and second lowest lattice band is of order $4E_L$

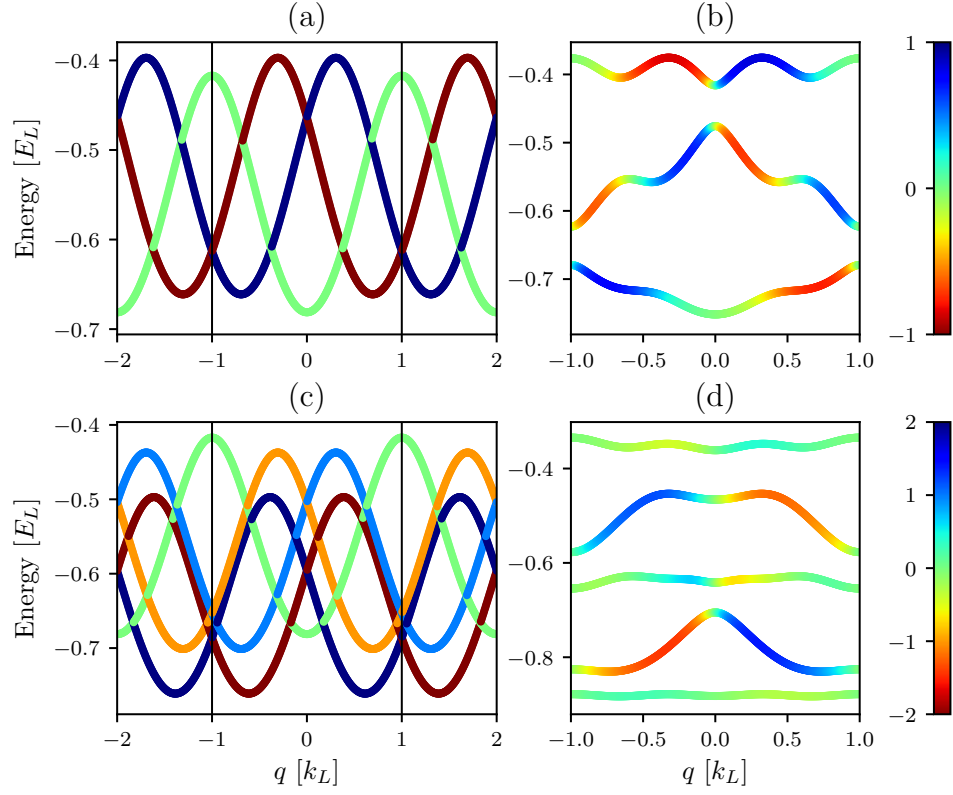


Figure 2: Band structure of the synthetic dimensions Hamiltonian, eqn. 6.4. For all panels, the detuning $\hbar\delta = 0$ and the quadratic shift $\hbar\epsilon = 0.02E_L$. (a) $F = 1$, $\hbar\Omega = 0.0$. (b) $F = 1$, $\hbar\Omega = 0.5$. (c) $F = 2$, $\hbar\Omega = 0.0$. (d) $F = 2$, $\hbar\Omega = 0.5$.

(see Figure 2), while the width of the lowest band, given by the amplitude of the approximate sinusoid, is of order $0.3E_L$ for our range of lattice depths, around $5.0E_L$. As long as the Raman coupling stays small compared to the lattice band spacing, the higher lattice bands are energetically separated enough that they can be ignored.

Therefore, we can think of the Raman coupling analogously to the free space Raman coupling (see section 2.4.3), except instead of free space parabolas each spin state gets a lowest lattice band sinusoid. Figure 2a shows this in the limit of no Raman coupling, $\Omega = 0$, but with the lattice on at $V_0 = 4.0E_L$. The quadratic Zeeman shift is $\hbar\epsilon = 0.02E_L$ and the detuning $\delta = 0$. The $m_F = -1$ sinusoid is shifted $2k_R$, similarly to section 2.4.3, but since the sinusoid is periodic with $2k_L$, it folds into the first Brillouin zone of the lattice, such that the nearest minimum to $q = 0$ is at $q = 2k_R - 2k_L = (2\phi_{AB}/2\pi - 2)k_L$. The edges of the Brillouin zone are marked by horizontal lines. The color indicates magnetization $\langle m \rangle = \sum_{m_F} m_F n_{m_F}$, where n_{m_F} is the fractional population in the m_F state. In synthetic dimensions language, $\langle m \rangle$ is the expectation value of position along \mathbf{e}_s .

In Figure 2b, we have restricted ourselves to the first Brillouin zone and turned on the Raman coupling to $\hbar\Omega = 0.5E_L$. The crossings of the bands in Figure 2a become avoided crossings, and the lowest band now has a spin dependence on crystal momentum. Figure 2c-d shows the same progression for the $F = 2$ manifold. Figure 2c is taken in the limit of $\hbar\Omega = 0.0$. All of the 5 spin states get 'folded' back into the first Brillouin zone due to the lattice periodicity of the bands. The different heights of the sinusoids are due to the quadratic Zeeman shift $\hbar\epsilon = 0.02E_L$. The lattice depth is again $V_0 = 5.0E_L$ and detuning $\hbar\delta = 0$. In Figure 2d we have restricted ourselves to the first Brillouin zone and turned on the Raman coupling to $\hbar\Omega = 0.5E_L$. Note that the inverted hyperfine structure in 2c (meaning that the quadratic shift pushed the $m_F = 0$ state up rather than down in energy compared to the others), combined with the Raman coupling serves to make the lowest band

in the $F = 2$ manifold close to flat.

6.2.3 Calibration

To calibrate the lattice depth V_0 in the synthetic dimensions system, we can simply calibrate the lattice depth without Raman or rf coupling as described in Section 2.3.4. However, we are operating at very low Raman coupling strengths, $\hbar\Omega \approx 0.5E_L$. This is necessary because in the synthetic dimensional system the Raman coupling plays the role of tunneling, which has to be small to approximate the tight binding limit. At these low Raman couplings, simple pulsing as described in Section 2.4.4, as the contrast of the Rabi oscillations would be too low to resolve. Therefore, we calibrate the Raman coupling and detuning with the full synthetic dimensions system, where the 'folding in' effect of the lattice makes the higher Raman bands much closer energetically than without the lattice, leading to larger contrast and allowing for accurate calibration.

To do this, we must first adiabatically load the lowest 1-D lattice band. To do that, we must ramp on the lattice potential on a time scale slow compared to the band spacing, $\approx 4E_L$. This gives $t \approx \hbar/4E_L = 0.12$ ms. Figure 3a shows the full ramping scheme. We ramp the lattice on in ≈ 20 ms. Then, we must pulse on the Raman coupling on a time scale fast compared to the spin sub-band level spacing to produce Rabi oscillations, but still adiabatic with respect to the lattice spacing to avoid exciting to the higher lattice band. We ramp the Raman beams on in $300 \mu\text{s}$. Then, the system is held on for a variable amount of time before all light is snapped off and the atoms are allowed to expand in time-of-flight. For the case of $F = 2$ atoms, the transfer to the $F = 2$ manifold is done in the 1-D lattice before the Raman beams are ramped on to minimize the time spend in the $F = 2$ manifold.

Figure 3c,d shows sample time-of-flight images during the calibration proce-

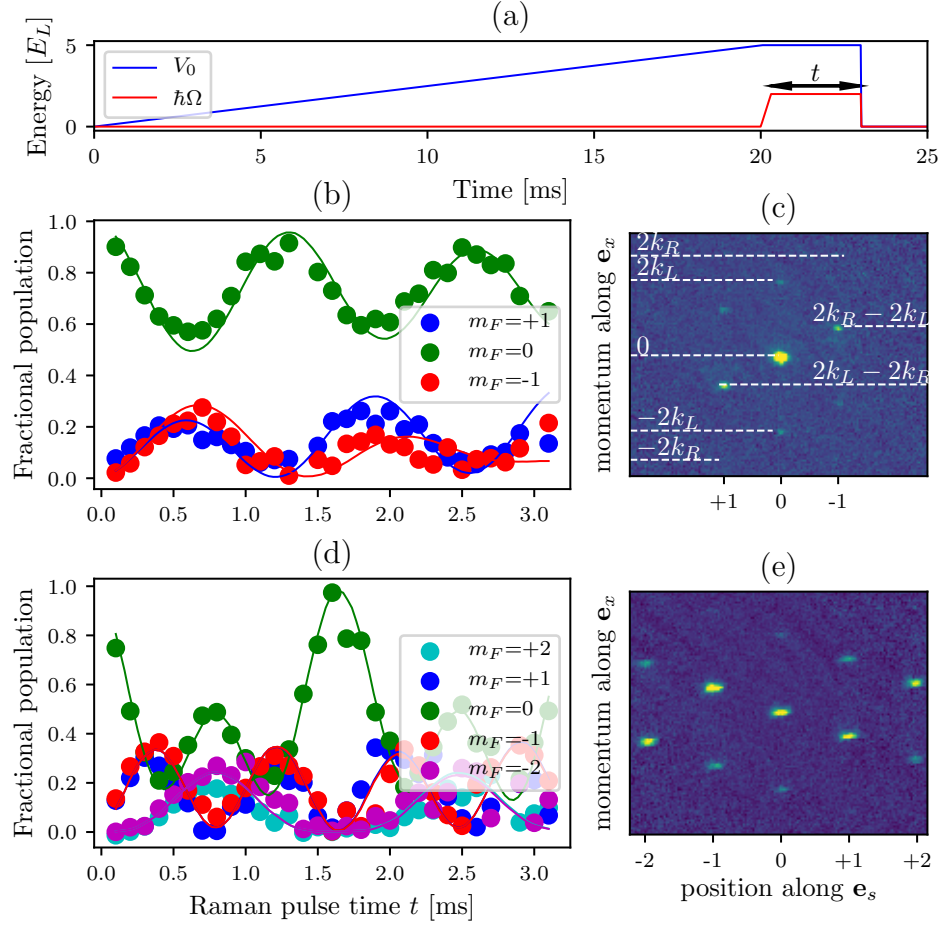


Figure 3: Calibration of synthetic dimensions lattice. (a) Ramping procedure. The blue line represents the 1-D lattice depth as a function of time and the red line represents Raman coupling as a function of time. Both are held on for a variable amount of time t , producing Rabi oscillations. (b) Example of fractional populations in different m states as a function of time t in the $F = 1$ manifold. Dots indicate data and lines indicate the best fit to theory, with parameters $\hbar\Omega = 0.56 \pm 0.01 E_L$ and $\hbar\delta = 0.029 \pm 0.002 E_L$. (c) Example time-of-flight image in the $F = 1$ manifold. A Stern-Gerlach gradient pulse separates different m states along the horizontal axis, while the lattice and Raman beams give momentum along the vertical axis. (d) Example of fractional populations in different m states as a function of time t in the $F = 2$ manifold. Dots indicate data and lines indicate the best fit to theory, with parameters $\hbar\Omega = 0.61 \pm 0.002 E_L$ and $\hbar\delta = 0.002 \pm 0.001 E_L$. (e) Example time-of-flight image in the $F = 2$ manifold. A Stern-Gerlach gradient pulse separates different m states along the horizontal axis, while the lattice and Raman beams give momentum along the vertical axis.

ture for $F = 1$ and $F = 2$ respectively. The vertical axis is \mathbf{e}_x , aligned with the lattice and Raman beams. Since the atoms have expanded in time-of-flight, this axis corresponds to the momentum k_x . The horizontal axis of the image is the axis along which a Stern-Gerlach magnetic field gradient, separating the different spin states, is applied. Therefore, this axis is the position m along the synthetic dimension \mathbf{e}_s . In the effectively 2-D synthetic dimensions lattice language, this is a 'hybrid' imaging technique—imaging momentum along one lattice direction and position along the other.

Figure 3c labels some notable momentum orders. The central order is at $k_x = 0$, where the atoms start before the experiment. Two higher lattice orders, at $k_x = \pm 2k_L$, are populated for the same spin $m = 0$. $k_x = \pm 2k_R$ is labelled, but not visibly populated, to indicate where the orders would appear if only Raman coupling was present with a higher coupling strength. Due to the 'folding in' effect of the lattice, the brightest orders of the $m = \pm 1$ states appear at $k_x = \pm(2k_L - 2k_R)$. The $F = 2$ states follow the same pattern, not labelled in Figure 3e as there are too many orders.

For each value of the time t we sum up the total optical depth in all of the orders of each spin state to obtain fractional populations for each spin state as a function of time. An example scan in the $F = 1$ manifold is shown in Figure 3b. The colored dots represent the data for different spin states, and the lines represent the best fit to theory. Here, the significant detuning makes populations in the $m = \pm 1$ states unequal. An example scan in the $F = 2$ manifold is shown in Figure 3e. Here, the detuning is small and states with opposite spin oscillate in approximate unison.

6.2.4 Tight binding approximation

The synthetic dimensions Hamiltonian can be approximated in the tight binding limit as:

$$H = - \sum_{j,m} t_x e^{i\phi_{AB}m} |j+1, m\rangle \langle j, m| + t_s(m) |j, m+1\rangle \langle j, m| + A_m |j, m\rangle \langle j, m| + h.c., \quad (6.7)$$

where j and m label sites along \mathbf{e}_x and \mathbf{e}_s respectively, as shown in Figure 1b. $t_s = |t_s|$ and $t_x = |t_x| \exp(-i\phi_{AB}m)$ are the associated tunnelings. A_m captures the spin dependent diagonal elements, detuning $\hbar\delta$ and quadratic shift $\hbar\epsilon$. Here, we have implicitly restricted ourselves to the lowest 1-D lattice band, and assumed that tight binding, ie confinement at discrete lattice sites, is a good approximation (see 2.3.3). t_s is not a spin dependent quantity for $F = 1$ atoms, but is for $F = 2$, where differences in Clebsch-Gordan coefficients create non-uniform tunneling. In the limit of zero detuning and neglecting the quadratic shift as well as the t_s dependence on spin, this becomes the traditional Harper-Hofstadter Hamiltonian

$$H = - \sum_{j,m} t_x e^{i\phi_{AB}m} |j+1, m\rangle \langle j, m| + t_s |j, m+1\rangle \langle j, m| + h.c. \quad (6.8)$$

We can transform this Hamiltonian into momentum space along \mathbf{e}_x by plugging the Fourier transform formula

$$|j, m\rangle = \frac{1}{\sqrt{N}} \sum_{k_j} e^{-ik_j j} |k_j, m\rangle \quad (6.9)$$

into the above Hamiltonian to obtain

$$H = -\frac{1}{N} \sum_{k_j, m} t_m |k_j, m+1\rangle \langle k_j, m| + h.c. + 2t_x \cos(k_j - \phi_{AB}) |k_j, m\rangle \langle k_j, m| + A_m |k_j, m\rangle \langle k_j, m| \quad (6.10)$$

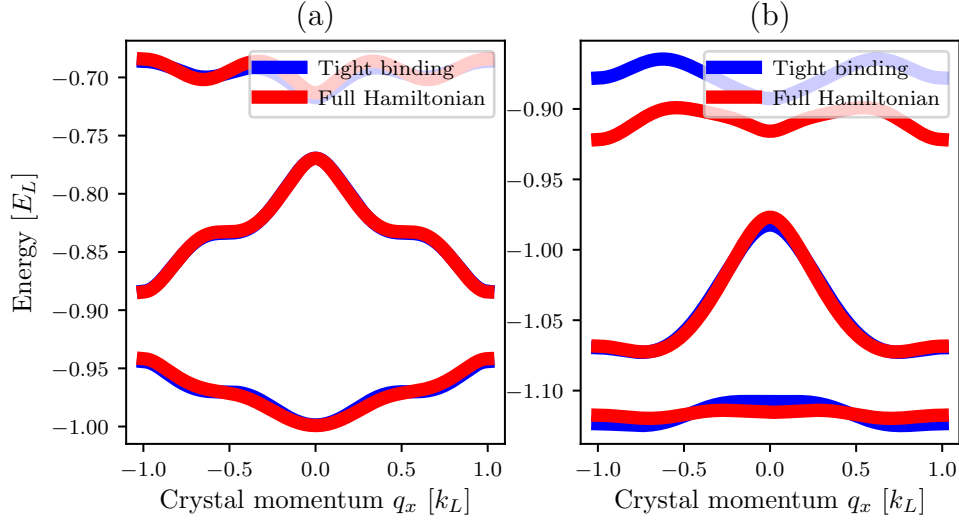


Figure 4: Band structure of the tight binding versus full Hamiltonian. $V_0 = 6.0E_L$, giving $t_x = 0.1E_L$, $\hbar\delta = 0$, $\hbar\epsilon = 0.02E_L$, $\hbar\Omega = 0.5E_L$. (a) $F = 1$, fitted value $t_s = 0.154E_L$. (b) $F = 2$, fitted value $t_s = 0.284$.

To go from the full Hamiltonian, eqn. 6.4, to the tight binding Hamiltonian we must find appropriate values for t_s and t_x . We find $|t_x|$ by treating the 1-D lattice independently, and matching the tight binding band to the lowest full lattice band. For most of the experiments described in the chapter, the lattice depth was $V_0 = 6E_L$, corresponding to $|t_x| \approx 0.01E_L$. To find the appropriate value of t_s , we fit the full synthetic dimensions band structure to the tight binding band structure eqn. 6.10 with t_s as a free parameter.

=====

The band structure of this Hamiltonian is presented in Figure 2. Here, we have restricted ourselves to the lowest lattice band. We can do this because the energy splitting between the lowest and second lowest lattice band is of order $4E_L$ (see Figure 2), while the width of the lowest band, given by the amplitude of the approximate sinusoid, is of order $0.3E_L$ for our range of lattice depths, around $5.0E_L$. As long as the Raman coupling stays small compared to the lattice band spacing, the higher lattice bands are energetically separated enough that they can be ignored.

Therefore, we can think of the Raman coupling analogously to the free space Raman coupling (see section 2.4.3), except instead of free space parabolas each spin state gets a lowest lattice band sinusoid. Figure 2a shows this in the limit of no Raman coupling, $\Omega = 0$, but with the lattice on at $V_0 = 4.0E_L$. The quadratic Zeeman shift is $\hbar\epsilon = 0.02E_L$ and the detuning $\delta = 0$. The $m_F = -1$ sinusoid is shifted $2k_R$, similarly to section 2.4.3, but since the sinusoid is periodic with $2k_L$, it folds into the first Brillouin zone of the lattice, such that the nearest minimum to $q = 0$ is at $q = 2k_R - 2k_L = (2\phi_{AB}/2\pi - 2)k_L$. The edges of the Brillouin zone are marked by horizontal lines. The color indicates magnetization $\langle m \rangle = \sum_{m_F} m_F * n_{m_F}$, where n_{m_F} is the fractional population in the m_F state. In synthetic dimensions language, $\langle m \rangle$ is the expectation value of position along \mathbf{e}_s .

In Figure 2b, we have restricted ourselves to the first Brillouin zone and turned on the Raman coupling to $\hbar\Omega = 0.5E_L$. The crossings of the bands in Figure 2a become avoided crossings, and the lowest band now has a spin dependence on crystal momentum. Figure 2c-d shows the same progression for the $F = 2$ manifold. Figure 2c is taken in the limit of $\hbar\Omega = 0.0$. All of the 5 spin states get 'folded' back into the first Brillouin zone due to the lattice periodicity of the bands. The different heights of the sinusoids are due to the quadratic Zeeman shift $\hbar\epsilon = 0.02E_L$. The lattice depth is again $V_0 = 5.0E_L$ and detuning $\hbar\delta = 0$. In Figure 2d we have restricted ourselves to the first Brillouin zone and turned on the Raman coupling to $\hbar\Omega = 0.5E_L$. Note that the inverted hyperfine structure in 2c (meaning that the quadratic shift pushed the $m_F = 0$ state up rather than down in energy compared to the others), combined with the Raman coupling serves to make the lowest band in the $F = 2$ manifold close to flat.

6.2.5 Calibration

To calibrate the lattice depth V_0 in the synthetic dimensions system, we can simply calibrate the lattice depth without Raman or rf coupling as described in Section 2.3.4. However, we are operating at very low Raman coupling strengths, $\hbar\Omega \approx 0.5E_L$. This is necessary because in the synthetic dimensional system the Raman coupling plays the role of tunneling, which has to be small to approximate the tight binding limit. At these low Raman couplings, simple pulsing as described in Section 2.4.4, as the contrast of the Rabi oscillations would be too low to resolve. Therefore, we calibrate the Raman coupling and detuning with the full synthetic dimensions system, where the 'folding in' effect of the lattice makes the higher Raman bands much closer energetically than without the lattice, leading to larger contrast and allowing for accurate calibration.

6.2.6 Tight binding approximation

~~~~~ c97331a66b85a2b571b002e6f35db25273edc050

Figure 4 shows the overlayed band structure of the full Hamiltonian, eqn. 6.4, and the best fit tight binding band structure, eqn. 6.10. To fit, we minimize the square difference between the energies in the lowest two bands, relevant to our experiment.

## 6.3 Eigenstates of the synthetic 2-D lattice

After calibrating the synthetic dimensional lattice via pulsing, we can study the eigenstates of the lowest band of the system by adiabatically loading, i.e. ramping both the lattice and Raman or rf coupling on on a time scale slow compared to the magnetic band spacing. Along the synthetic direction, in the  $F = 1$  manifold, there are no  $m = \pm 2$  sites. This can be thought of as hard wall boundary conditions at

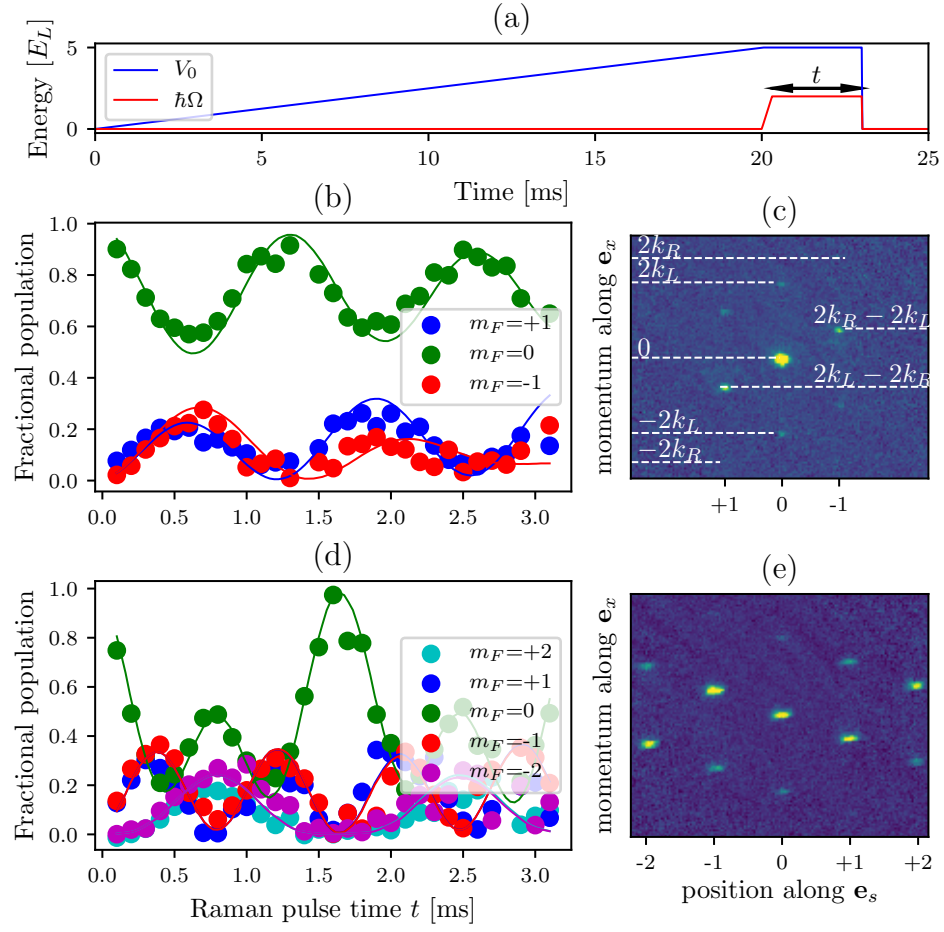


Figure 5:

the  $m = \pm 2$  sites, confining the atoms in the allowed  $m = 0, \pm 1$  sites. Therefore, we can consider the position eigenstates along the synthetic direction in relation to eigenstates of a square well potential.

Figure 5a shows a time-of-flight image of an adiabatically loaded synthetic dimensions lattice eigenstate with rf coupling along the synthetic direction. The vertical axis is single site resolved spin states  $m$ . The horizontal axis is momentum along the  $\mathbf{e}_x$  direction. Note that for each site  $m$  the distribution of momenta  $k_x$  is symmetric. Figure 5b shows the fractional population in each site  $m$ , summed over all momenta  $k_x$ . In the case of rf coupling,  $\phi_{AB} = 0$  and the effective magnetic flux  $\Phi_{AB}/\Phi_0 = 0$ . Therefore, the fractional population along the spin direction looks simply like a discretized ground state probability distribution of the square well potential.

Figure 5c-h shows analogous data with Raman coupling along the synthetic direction. Figure 5d,g are the time-of-flight image and corresponding fractional populations of atoms adiabatically loaded from the  $m_F = 0$  spin state, corresponding to the central minimum ( $q = 0$ ) of the lowest band in Figure 2b. There are two key differences between this case and the rf case Figure 5a-b. First, the momenta of the different spin states are no longer symmetric, as explained in sec. 6.2.3. Second, the fractional populations in Figure 5g are no longer simply the discretized ground state probability distribution of the square well potential—it is a narrowed version of it, more strongly concentrated in the  $m = 0$  site.

This can be understood by analogy with a 2D electron system in a perpendicular magnetic field, confined in one dimension with hard walls. Along the confined direction, the wavefunction is localized to the scale of the magnetic length  $l_B = \sqrt{\hbar/qB}$ , with the center position at  $k_x l_B^2$  in the bulk state, where  $\hbar k_x$  is the electrons canonical momentum. In our system, the magnetic length  $l_B = \sqrt{a^2 \Phi_0 / 2\pi \Phi_{AB}}$ , or in units of the lattice period  $a$ ,  $l_B^* = \sqrt{3/2\pi}$ ; this explains the narrowing of the

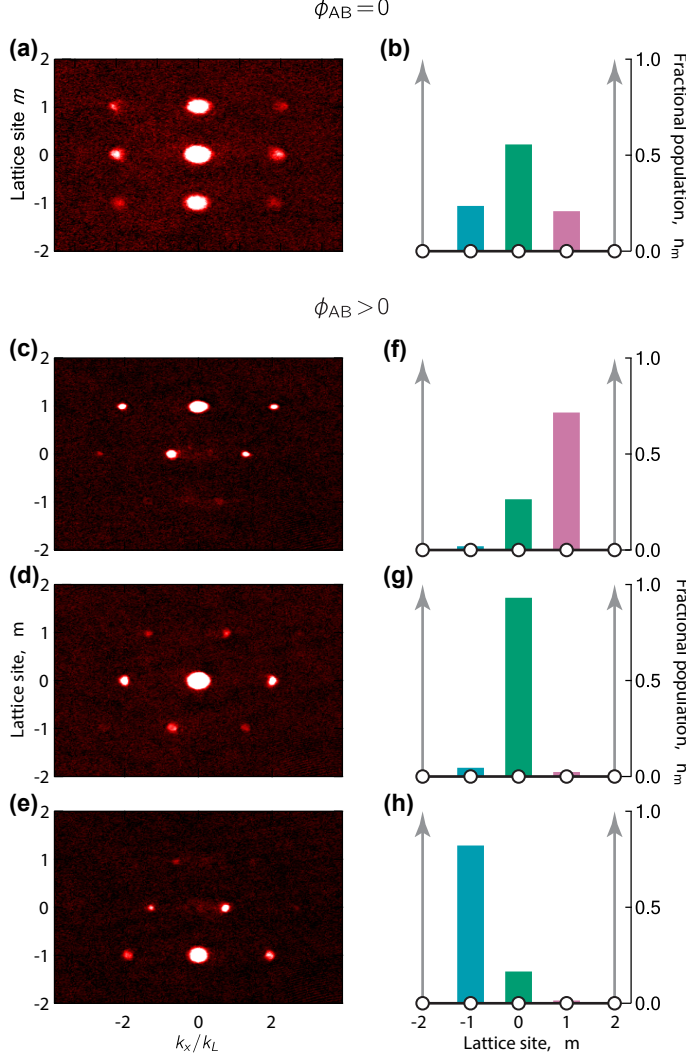


Figure 6: Eigenstates of the synthetic dimensions lattice. Left column: time-of-flight images, with position along  $\mathbf{e}_s$  on the vertical axis and momentum along  $\mathbf{e}_s$  on the horizontal. Right column: fractional populations in each site  $m$ . (a,b) Rf coupling, resulting in  $\phi_{AB} = 0$ . (c,f) Raman coupling, resulting in  $\phi_{AB} > 0$ , adiabatically loaded from the  $m_F = 1$  state. (d,g) Raman coupling, resulting in  $\phi_{AB} > 0$ , adiabatically loaded from the  $m_F = 0$  state. (e,h) Raman coupling, resulting in  $\phi_{AB} > 0$ , adiabatically loaded from the  $m_F = -1$  state.

bulk state in Figure 5g.

In the 2D electron system, at large  $|k_x|$ , the electron becomes localized near the edges, lifting the degeneracy of the otherwise macroscopically degenerate Landau levels. In our case, stable edge states appeared as the additional minima in Figure 2b, at  $q \approx \pm 0.66k_L$ . We loaded these edge states by starting in the  $m_F = \pm 1$  states before adiabatically turning on the synthetic dimensions lattice to obtain eigenstates displayed in Figure 5c,f and Figure 5e,h respectively. These edge states predominantly occupy the edge sites in the synthetic direction, and are strongly confined there due to the narrow magnetic length. These localized edge states are the analog to the current-carrying edge states in fermionic integer quantum Hall effect systems [24].

## 6.4 Chiral edge currents

The same pulsing procedure that was used for calibration (sec. 6.2.3) can also be interpreted by analogy with the 2-D electron system. Figure 6a shows schematically what happens atoms are loaded from the  $m = 0$  site into the lattice and tunneling along the synthetic dimension is pulsed on. Atoms begin analogues of cyclotron orbits, tunneling out into the edge  $m = \pm 1$  sites and tunneling back to the bulk  $m = 0$  state. The fractional populations in the three  $m$  sites as a function of time are shown in Figure 6b.

We performed this experiment for three different magnetic flux values: with rf coupling giving  $\Phi_{AB}/\Phi_0 = 0$ , with Raman coupling giving  $\Phi_{AB}/\Phi_0 \approx 4/3$  and with inverted Raman coupling giving  $\Phi_{AB}/\Phi_0 \approx -4/3$ . The inverted Raman coupling was accomplished by switching the roles of the two Raman beams (see Figure ??a): the right going beam frequency was changed to  $2\pi(\omega + \Delta\omega)$  and the left going beam frequency to  $2\pi\omega$ , resulting in the opposite recoil momentum for the same spin flip, flipping the direction of the effective magnetic field.

We define the current  $I_{m=\pm 1} = n_m \langle v_m \rangle$ , where  $n_m$  is the fractional population in site  $m$  and  $\langle v_m \rangle$  is the expectation value of velocity along  $\mathbf{e}_x$  for atoms in sites  $m$ , as depicted in Figure 6a. The velocity is derived from the momentum measured in time-of-flight images. The chiral current of the system is then defined as  $\mathcal{I} = I_1 - I_{-1}$ . We calculate this chiral current for data in Figure 6b, with  $\Phi_{AB}/\Phi_0 \approx 4/3$ , displayed in red dots in Figure 6c. Atoms in the edge sites  $m = \pm 1$  exhibit chiral motion, therefore the resulting chiral current is directly proportional to the fractional population in those sites and oscillates as a function of time in concert with the oscillation in Figure 6b. in Figure 6c also includes data for the  $\Phi_{AB}/\Phi_0 \approx -4/3$  (solid black dots indicate data and solid black lines are from theory) and  $\Phi_{AB}/\Phi_0 = 0$  (empty black dots). As seen in the figure, reversing the direction of the effective magnetic flux reverses the direction of the chiral current, and turning off the magnetic flux results in no net chiral current. The chiral current  $\mathcal{I}$  is normalized here by the tunneling velocity  $2t_x/\hbar k_L$ .

As the chiral current  $\mathcal{I}$  is proportional to the edge state population, we plot it as a function of the expectation value of the absolute value of  $m$ ,  $\langle |m| \rangle$ , in Figure 6d. As expected, the chiral current is linear and positive for  $\Phi_{AB}/\Phi_0 \approx 4/3$ , negative for  $\Phi_{AB}/\Phi_0 \approx -4/3$ , and zero for  $\Phi_{AB}/\Phi_0 = 0$ . We call this slope  $\mathcal{S}$ . We then study the dependence of the chiral current on the strength of tunneling along the synthetic dimension, in units of the real axis tunneling  $t_s/t_x$ . We refer to this as the tunneling anisotropy: the asymmetry between the two dimensions. As shown in the inset to Figure 6e, the slope  $\mathcal{S}$  of the chiral current as a function of  $\langle |m| \rangle$  is practically independent of the tunneling anisotropy. The small deviation from a flat line is explained by the deviation of our system from the tight binding model. However, the maximal chiral current attained during the pushing experiment,  $\mathcal{I}_{\max}$ , depends strongly on the tunneling anisotropy (see Figure 6e). This is because the maximum fractional population in the edge states  $\langle |m| \rangle$  increases with increased  $t_s$ .



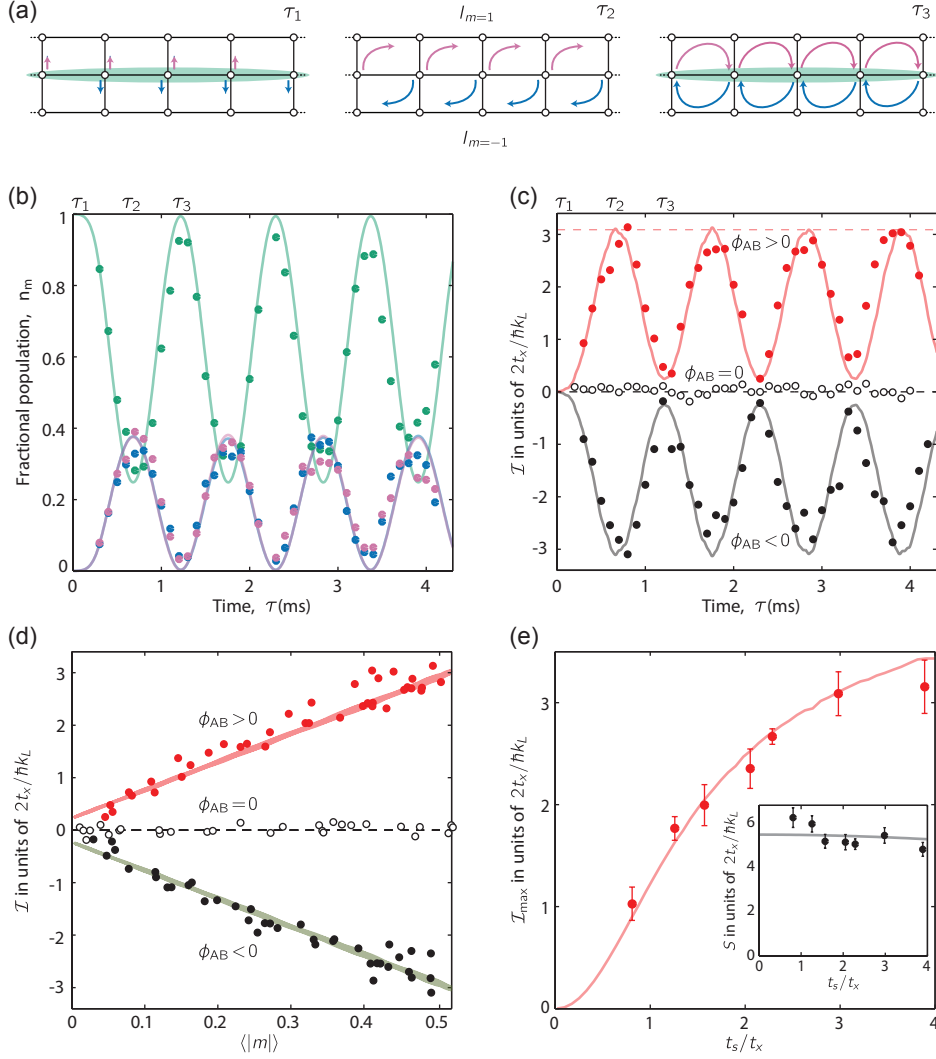


Figure 7: Measuring chiral currents in synthetic dimensions. (a) Schematic of the formation of chiral currents when the system is loaded into the bulk  $m = 0$  site and tunneling along  $\mathbf{e}_s$  is turned on suddenly. (b) Fractional population in each spin state as a function of time for a system with  $\phi_{AB} > 0$ . Dots represent data and lines represent theory, with parameters  $\hbar\Omega = 0.5E_L$ ,  $V_0 = 6E_L$ ,  $\hbar\delta = 0.001E_L$ , and  $\hbar\epsilon = 0.05E_L$ . (c) Chiral current  $\mathcal{I}$  as a function of time for  $\phi_{AB} > 0$  (red)  $\phi_{AB} = 0$  (empty black dots) and  $\phi_{AB} < 0$  (solid black). (d) Chiral current  $\mathcal{I}$  as a function of  $\langle |m| \rangle$  for the three values of  $\phi_{AB}$ . Solid lines calculated from theory, with the same parameters as in (b) for  $\phi_{AB} \neq 0$ , and with parameters  $\hbar\Omega = 0.33E_L$ ,  $V_0 = 6E_L$ ,  $\hbar\delta = -0.01E_L$ , and  $\hbar\epsilon = 0.05E_L$  for  $\phi_{AB} = 0$ . (e) Peak chiral current  $\mathcal{I}_{\max}$  as a function of tunneling asymmetry  $t_s/t_x$ . Inset: slope of best fit lines of current  $\mathcal{I}$  as a function of  $\langle |m| \rangle$  (as in (d)) as a function of tunneling asymmetry  $t_s/t_x$ : nearly independent.

The increase is approximately linear at first, and then saturates at large  $t_s/t_x$  when the fractional population in the edge states  $m = \pm 1$  approaches 1.

## 6.5 Chiral edge currents

## 6.6 Observation of skipping orbits

Semiclassically, electrons in a 2-D material pierced by a magnetic field can be described in terms of cyclotron orbits in the bulk, as described in the previous section, and skipping orbits on the edge. Skipping orbits arise from electrons on the edge beginning cyclotron orbits, but hitting the edge of the system and being reflected and beginning the next cyclotron orbit. Due to the chirality of the cyclotron orbits, this results in the skipping orbits travelling in one direction along the top edge and in the opposite direction along the bottom edge.

We observed an analogue of these skipping orbits in our system. We performed the same experiment, pulsing on tunneling along the synthetic dimension, but this time initializing the system on the edge, as shown schematically in Figure 7a. To populate these states, we initially applied a detuning  $\hbar\delta = \pm 0.087E_L$ , tilting the potential along the synthetic direction as shown in Figure 7b. This made the initial state,  $m = -1$  in the figure, a potential minimum. We then pulsed on the tunneling and observed the resulting dynamics.

Figure 7c shows the expectation value of position along  $\mathbf{e}_s$  as a function of time during the pulsing experiment. This expectation value is obtained by calculating the fractional population  $n_m$  on each site  $m$  and summing  $\langle m \rangle = \sum_m m n_m$ . The red dots were obtained from an experiment where the atoms were initialized in the  $m = 1$  site. The blue dots were obtained by starting in the  $m = -1$  site. The expected position oscillated with time, as expected for Rabi oscillations. The same data was then used to extract the expected group velocity along  $\mathbf{e}_x$ ,  $\langle v \rangle = \sum_m n_m \langle v_m \rangle$  as a

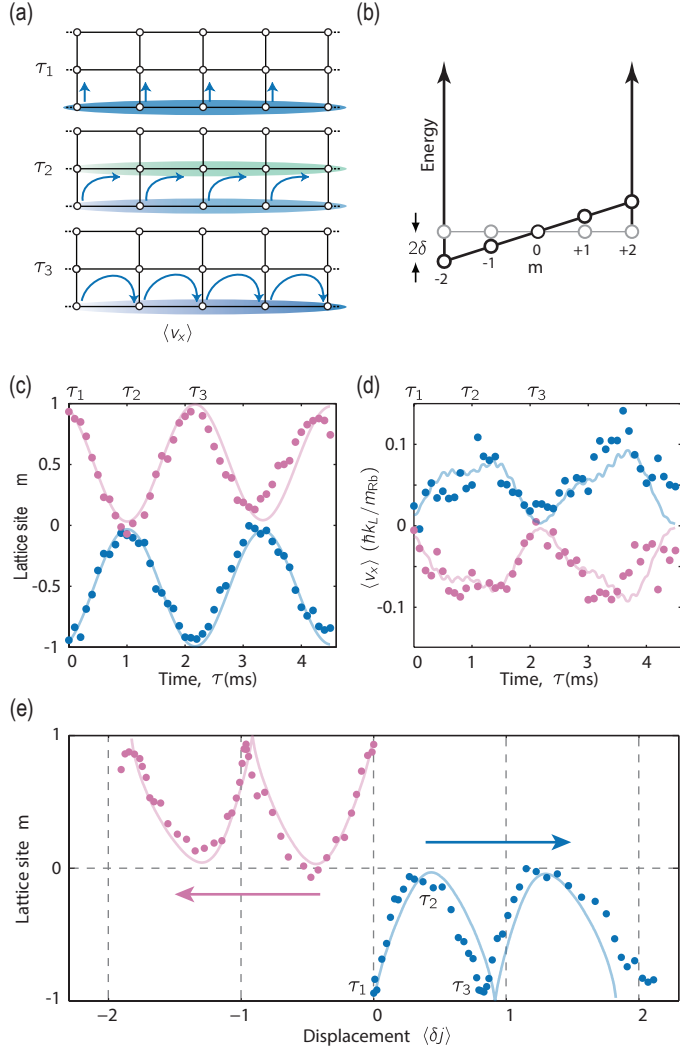


Figure 8: Imaging skipping orbits. (a) Schematic of pulsing experiment when atoms are initialized on the edge. (b) Schematic of the tilted box potential applied along the synthetic direction. (c) Expectation value of position along  $\mathbf{e}_s$ ,  $\langle m \rangle$ , as a function of pulse time for atoms initialized in the  $m = +1$  (red) and  $m = -1$  (blue) states. Dots represent data and lines are from theory with parameters  $\hbar\Omega = 0.41E_L$ ,  $V_0 = 5.2E_L$ ,  $\hbar\delta = \pm 0.087E_L$ , and  $\hbar\epsilon = 0.13E_L$ . (d) Expectation value of the group velocity along  $\mathbf{e}_x$ ,  $\langle v_x \rangle$ , for the same data as in (c). (e) Expectation value of displacement along  $\mathbf{e}_x$ ,  $\langle \delta j \rangle$  in units of lattice spacing, for the same data as in (c) and (d). The displacement was obtained by integrating  $\langle v_x/a \rangle$ , where  $a$  is the period of the optical lattice. Atoms initialized in  $m = -1$  performed skipping orbits to the left, while atoms starting in  $m = +1$  travelled to the right.

function of time. This is shown in Figure 7d. The group velocity oscillated with the expected position  $\langle m \rangle$ , and was positive for experiments starting in  $m = -1$  and negative for experiments starting in  $m = 1$ .

We obtain the expected displacement in units of the lattice spacing  $a$ ,  $\langle \delta j \rangle$  along  $\mathbf{e}_x$  as a function of time by directly integrating the expected group velocity. The resulting displacement is shown in Figure 7e. As seen in the figure, for experiments initialized in  $m = 1$ , the atoms began cyclotron orbits, but reflected off the edge and performed skipping orbits towards the left. Likewise, atoms initialized in  $m = -1$  performed skipping orbits along the opposite edge and in the opposite direction. This experiment presents the first direct observation of skipping orbit motion.

## Bibliography

- [1] Daniel Adam Steck. Rubidium 87 d line data. Available online, <http://steck.us/alkalidata>, April 2018. revision 2.1.5.
- [2] K. Jiménez-García, L. J. LeBlanc, R. A. Williams, M. C. Beeler, A. R. Perry, and I. B. Spielman. Peierls substitution in an engineered lattice potential. *Phys. Rev. Lett.*, 108:225303, May 2012.
- [3] H.J. Metcalf and P. van der Straten. *Laser Cooling and Trapping*. Graduate Texts in Contemporary Physics. Springer New York, 1999.
- [4] N.W. Ashcroft and N.D. Mermin. *Solid State Physics*. Saunders College, Philadelphia, 1976.
- [5] Nicola Marzari, Arash A. Mostofi, Jonathan R. Yates, Ivo Souza, and David Vanderbilt. Maximally localized wannier functions: Theory and applications. *Rev. Mod. Phys.*, 84:1419–1475, Oct 2012.
- [6] Karina Jimenez-Garcia. *Artificial Gauge Fields for Ultracold Neutral Atoms*. PhD thesis, Joint Quantum Institute, National Institute of Standards and Technology, and the University of Maryland, 2012.

- [7] Daniel Adam Steck. Quantum and atom optics. Available online at <http://steck.us/teaching>, January 2015. revision 0.12.2.
- [8] K. v. Klitzing, G. Dorda, and M. Pepper. New method for high-accuracy determination of the fine-structure constant based on quantized hall resistance. *Phys. Rev. Lett.*, 45:494–497, Aug 1980.
- [9] D. J. Thouless, M. Kohmoto, M. P. Nightingale, and M. den Nijs. Quantized hall conductance in a two-dimensional periodic potential. *Phys. Rev. Lett.*, 49:405–408, Aug 1982.
- [10] Douglas R. Hofstadter. Energy levels and wave functions of bloch electrons in rational and irrational magnetic fields. *Phys. Rev. B*, 14:2239–2249, Sep 1976.
- [11] M. C. Geisler, J. H. Smet, V. Umansky, K. von Klitzing, B. Naundorf, R. Ketzmerick, and H. Schweizer. Detection of a landau band-coupling-induced rearrangement of the hofstadter butterfly. *Phys. Rev. Lett.*, 92:256801, Jun 2004.
- [12] B. Hunt, J. D. Sanchez-Yamagishi, A. F. Young, M. Yankowitz, B. J. LeRoy, K. Watanabe, T. Taniguchi, P. Moon, M. Koshino, P. Jarillo-Herrero, and R. C. Ashoori. Massive Dirac Fermions and Hofstadter Butterfly in a van der Waals Heterostructure. *Science*, 340:1427, 2013.
- [13] P. Zoller D. Jaksch. Creation of effective magnetic fields in optical lattices: the hofstadter butterfly for cold neutral atoms. *New Journal of Physics*, 5(1):56, 2003.
- [14] M. Aidelsburger, M. Atala, M. Lohse, J. T. Barreiro, B. Paredes, and I. Bloch. Realization of the hofstadter hamiltonian with ultracold atoms in optical lattices. *Phys. Rev. Lett.*, 111(18):185301–, October 2013.

- [15] Hirokazu Miyake, Georgios A. Siviloglou, Colin J. Kennedy, William Cody Burton, and Wolfgang Ketterle. Realizing the harper hamiltonian with laser-assisted tunneling in optical lattices. *Phys. Rev. Lett.*, 111:185302, Oct 2013.
- [16] Gregor Jotzu, Michael Messer, Remi Desbuquois, Martin Lebrat, Thomas Uehlinger, Daniel Greif, and Tilman Esslinger. Experimental realization of the topological haldane model with ultracold fermions. *Nature*, 515(7526):237–240, Nov 2014.
- [17] M Aidelsburger, M Lohse, C Schweizer, M Atala, J T Barreiro, S Nascimbène, N. R. Cooper, I. Bloch, and N. Goldman. Measuring the Chern number of Hofstadter bands with ultracold bosonic atoms. *Nature Physics*, 11(2):162–166, December 2014.
- [18] M. Mancini, G. Pagano, G. Cappellini, L. Livi, M. Rider, J. Catani, C. Sias, P. Zoller, M. Inguscio, M. Dalmonte, and L. Fallani. Observation of chiral edge states with neutral fermions in synthetic hall ribbons. *Science*, 349(6255):1510–, Sep 2015.
- [19] M Hafezi, S Mittal, J Fan, A Migdall, and J M Taylor. Imaging topological edge states in silicon photonics. *Nat. Photon.*, 7(12):1001–1005, October 2013.
- [20] A. Celi, P. Massignan, J. Ruseckas, N. Goldman, I.B. Spielman, G. Juzeliunas, and M. Lewenstein. Synthetic gauge fields in synthetic dimensions. *Phys. Rev. Lett.*, 112(4):043001–, Jan 2014.
- [21] B. K. Stuhl, H.-I. Lu, L. M. Ayccock, D. Genkina, and I. B. Spielman. Visualizing edge states with an atomic bose gas in the quantum hall regime. *Science*, 349(6255):1514–, Sep 2015.
- [22] Y. Aharonov and D. Bohm. Significance of electromagnetic potentials in quantum theory. *Phys. Rev.*, 115:485, 1959.

- [23] Yakir Aharonov and Ady Stern. Origin of the geometric forces accompanying berry's geometric potentials. *Phys. Rev. Lett.*, 69(25):3593–3597, 1992.
- [24] Dario Hgel and Beln Paredes. Chiral ladders and the edges of quantum Hall insulators. *Phys. Rev. A*, 89(2):023619, 2014.